Unveiling the in-situ hydrogen intercalation in Mo_2CO_x for promoting the alkaline hydrogen evolution reaction

Hong Chuan Fu , Xiao Hui Chen , Bo Yang , Yuan Hao Luo , Ting Li , Xiao Hu Wang , Qing Zhang , Xiao Lin Li , Nian Bing Li [*], Hong Qun Luo [*]

School of Chemistry and Chemical Engineering, Southwest University, Chongqing 400715, People's Republic of China

ARTICLE INFO

ABSTRACT

Dimolybdenum carbide (Mo_2C) is an efficient electrocatalyst for the hydrogen evolution reaction (HER). However, Mo_2C tends to undergo surface chemical reconstruction under reaction conditions, which presents difficulties for optimization and characterization. Here, we report an HER activated Mo_2CO_x–$Ni(OH)_2$ catalyst and demonstrate that structural transformations including the surface oxidation of Mo_2C and the in-situ hydrogen intercalation of Mo_2CO_x govern the promoted HER performance. The electrochemically induced hydrogen intercalation from Mo_2CO_x to $H_xMo_2CO_x$ was identified by in-situ cyclic voltammetry characterization, and the significant role of hydrogen intercalation in surface-mediated HER pathway has been revealed by in-situ electrochemical impedance characterization. Density functional theory calculations indicate that hydrogen intercalation enables the HER by addressing sluggish water dissociation toward fast kinetics. Overall, this work underscores the importance of tracking the structure dynamic alteration of Mo_2C-based material under the reaction conditions.

1. Introduction

Alkaline HER has long been envisioned as a promising strategy for the future sustainable hydrogen energy [1–5]. In general, alkaline HER process features three fundamental reactions: the Volmer reaction ($H_2O + M + e^- \leftrightarrows M\text{-}H^* + OH^-$), and the Heyrovsky reaction ($H_2O + M\text{-}H^* + e^- \leftrightarrows M + H_2 + OH^-$) or the Tafel recombination reaction ($2\ M\text{-}H^* \leftrightarrows 2\ M + H_2$) [6,7]. Therefore, it is quite reasonable to conclude that the sluggish alkaline HER kinetics are caused by the extra water dissociation energy barrier. In this regard, Markovic et al. performed systematic experiments on Pt–$M_{2+\delta}O_\delta(OH)_{2-\delta}$ system (M = Ni, Co, Fe), revealing that $M_{2+\delta}O_\delta(OH)_{2-\delta}$ species can serve as additional water dissociation sites [8,9]. To date, the bifunctional theory derived from the Pt–$M_{2+\delta}O_\delta(OH)_{2-\delta}$ system works effectively in practice as the design principle for alkaline HER catalysts [10–12]. However, unlike the well-documented acidic HER, the real cause of the slow kinetics for alkaline HER stays controversial due to the multi-step reaction mechanism. Other influential factors such as the hydrogen binding energy (HBE) [13–16], potential of zero free charge (pzfc) [17,18], and the adsorbed hydroxyl transfer kinetic ($OH^* + e^- \leftrightarrow OH^-$) [19,20] have also been reported. Therefore, when using the bifunctional theory to

construct Pt–$M_{2+\delta}O_\delta(OH)_{2-\delta}$-like catalysts, we should be more rigorous to understand the real cause of the promoted HER performance, instead of simply copying Pt–$M_{2+\delta}O_\delta(OH)_{2-\delta}$-derived bifunctional mechanism.

Dimolybdenum carbide (Mo_2C) has long been advocated as a promising HER catalyst benefiting from its Pt-like electronic structure [21–25]. However, despite its popularity, pure Mo_2C binds quite strongly with hydrogen because of the high density of the empty d orbit of Mo, which hinders the desorption of the active hydrogen. So far, doping or hybridizing works effectively in further ameliorating the performance of Mo_2C-based materials, and in most cases, HBE is regarded as the sole descriptor [26–29]. Very recently, some researchers noticed that Mo_2C has a strong affinity with O-groups even at rather negative potentials [30–32]. On the one hand, this suggests that the surface Mo_2C is prone to oxidation, which can result in a surface reconstruction during HER process. On the other hand, the adsorption of O-intermediates (H_2O^* and OH^*) competes with H^* on the active sites during HER, and thus the strong affinity between Mo_2C and O-groups becomes influential to the activity. Thus, when using bifunctional theory to construct Mo_2C–$Ni(OH)_2$-like catalyst, multiple factors (e.g., surface reconstruction and O-intermediates adsorption behavior) should be considered simultaneously to explain the associated alteration of HER

---

activity.

Here, we report an HER activated Mo_2CO_x–$Ni(OH)_2$ catalyst that affords current density of 10 mA cm^{-2} at an overpotential of only 66 mV, which is much better than that (119 mV) of no-activated one. Different from the well-conducted bifunctional theory, in which only water dissociation effect of $Ni(OH)_2$ is highlighted, our work demonstrates the electrodeposition of $Ni(OH)_2$ triggers Mo_2C oxidation, which endows Mo_2CO_x undergoes further hydrogen intercalation in the following HER, and reveals that the promoted activity should not be simply ascribed to the bifunctional theory, but the hydrogen intercalation during HER. In-situ cyclic voltammetry combined with multiple characterizations identified the electrochemically-driven hydrogen intercalation of Mo_2CO_x–$Ni(OH)_2$ to $H_xMo_2CO_x$–$Ni(OH)_2$, along with the promoted HER performance. As revealed by density functional theory (DFT) calculations, the hydrogen intercalation enables the HER by reducing adsorption free energies of the O-intermediates (H_2O^* and OH^*) close to zero, thus accelerating water dissociation kinetics of the hybrid.

2. Results and discussion

Mo_2C supported on carbon cloth was fabricated via solvothermal growth and carbonization operations (Figs. S1 and S2). And the Mo_2C array well inherits the nanobelt array structure of MoO_x (Figs. S3-S5). Then, the Mo_2C–$Ni(OH)_2$ was obtained by a simple electrodeposition process. The optimal $Ni(OH)_2$ loading will be discussed later. As shown in Fig. S5, a sheet-like plating is grown on the Mo_2C, which indicates the successful construction of the hybrid structure. For a better comparison, MoS_2–$Ni(OH)_2$ system is also fabricated, and the corresponding X-ray diffraction (XRD) patterns and morphologies are shown in Figs. S6−S8. The alkaline HER performances for Mo_2C, MoS_2, Mo_2C–$Ni(OH)_2$, and MoS_2–$Ni(OH)_2$ were next tested, and the associated linear scan voltammetry (LSV) curves are shown in Fig. 1a. Typically, MoS_2–$Ni(OH)_2$

shows a better HER performance than MoS_2, conforming to the classic Pt–$Ni(OH)_2$ system. However, Mo_2C–$Ni(OH)_2$ displays a much higher overpotential of 119 mV to deliver the current density of 10 mA cm^{-2}, which is even worse than that of pure Mo_2C (106 mV), indicating that the activity of Mo_2C is even hindered after the introduction of $Ni(OH)_2$. Fig. 1b shows the p-t curves of Mo_2C–$Ni(OH)_2$ and MoS_2–$Ni(OH)_2$ at the constant current density of 10 mA cm^{-2}. Notably, the p-t curve of Mo_2C–$Ni(OH)_2$ at the first 2 h shows an obvious activation process (top of Fig. 1b), which suggests that a structural reconstruction of Mo_2C–Ni$(OH)_2$ may occur alongside the HER process. For comparison, the p-t curve of MoS_2–$Ni(OH)_2$ shows an obvious deactivation process (bottom of Fig. 1b), which indicates that such the activation process in Mo_2C–Ni$(OH)_2$ is not a common phenomenon in Pt–$Ni(OH)_2$ system derived catalysts. As shown in Fig. 1c, Mo_2C–$Ni(OH)_2$ after HER displays a remarkable HER performance with a quite low overpotential of only 66 mV to deliver 10 mA cm^{-2}. Therefore, it is attractive to understand the structural transformation for the above activation process. Note that the optimal $Ni(OH)_2$ loading has been discussed in Figs. S9 and S10 according to the activated Mo_2C–$Ni(OH)_2$ performance.

To probe the transformation, the XRD characterization was firstly employed to analyze the structural composition of the above catalysts. As shown in Fig. 2a, no new peaks can be observed for Mo_2C–$Ni(OH)_2$ and Mo_2C–$Ni(OH)_2$ after activation, which suggests that the newly electrodeposited $Ni(OH)_2$ is of low-crystallinity nature and the phase transformation of Mo_2C–$Ni(OH)_2$ during HER activation is quite subtle. The XRD pattern of bare carbon cloth with $Ni(OH)_2$ electrodeposited for 1 h is displayed in Fig. S11, which demonstrates the successful deposition of $Ni(OH)_2$ instead of metallic Ni. Therefore, transmission electron microscopy (TEM) characterization was conducted to try to gain further structural information. Obviously, the hierarchical $Ni(OH)_2$ sheets layer can be found in Fig. 2b, and the lattice spacing (0.23 nm) can be ascribed to the Mo_2C (101) plane in the high-resolution TEM image (Fig. 2c).
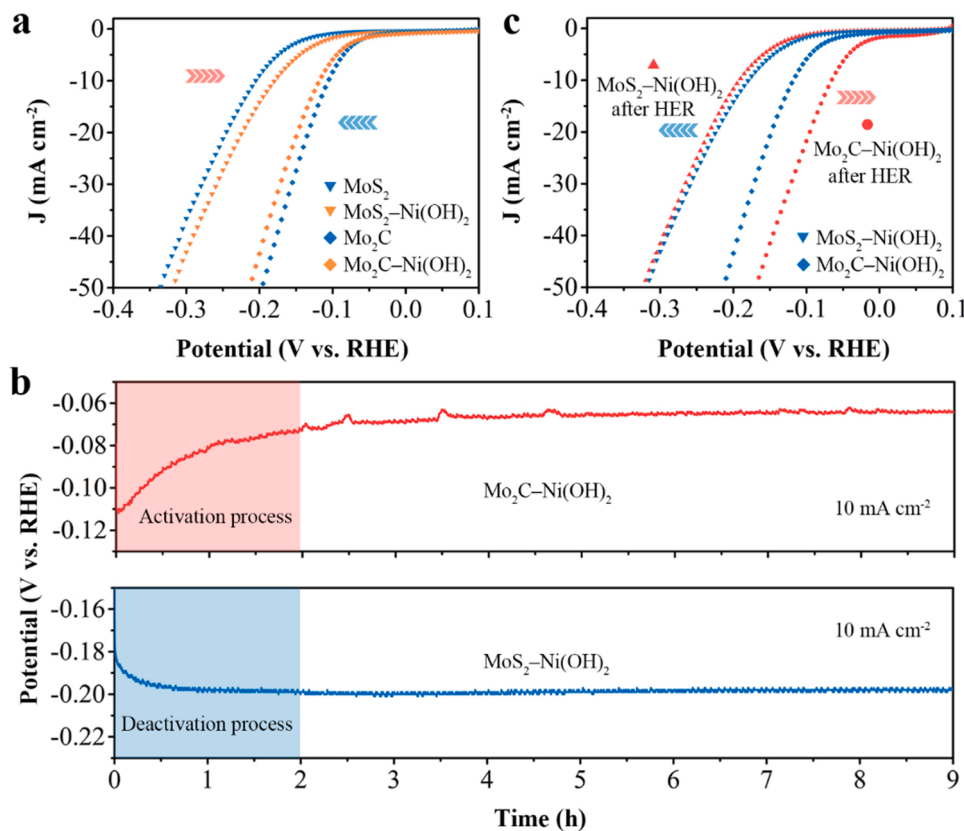

Fig. 1. (a) LSV curves of Mo_2C and MoS_2 before and after the electrodeposition. (b) P–t curves of Mo_2C–$Ni(OH)_2$ (top) and MoS_2–$Ni(OH)_2$ (bottom) at 10 mA cm^{-2} for 9 h. (c) LSV curves of Mo_2C–$Ni(OH)_2$ and MoS_2–$Ni(OH)_2$ after 9 h HER activation.
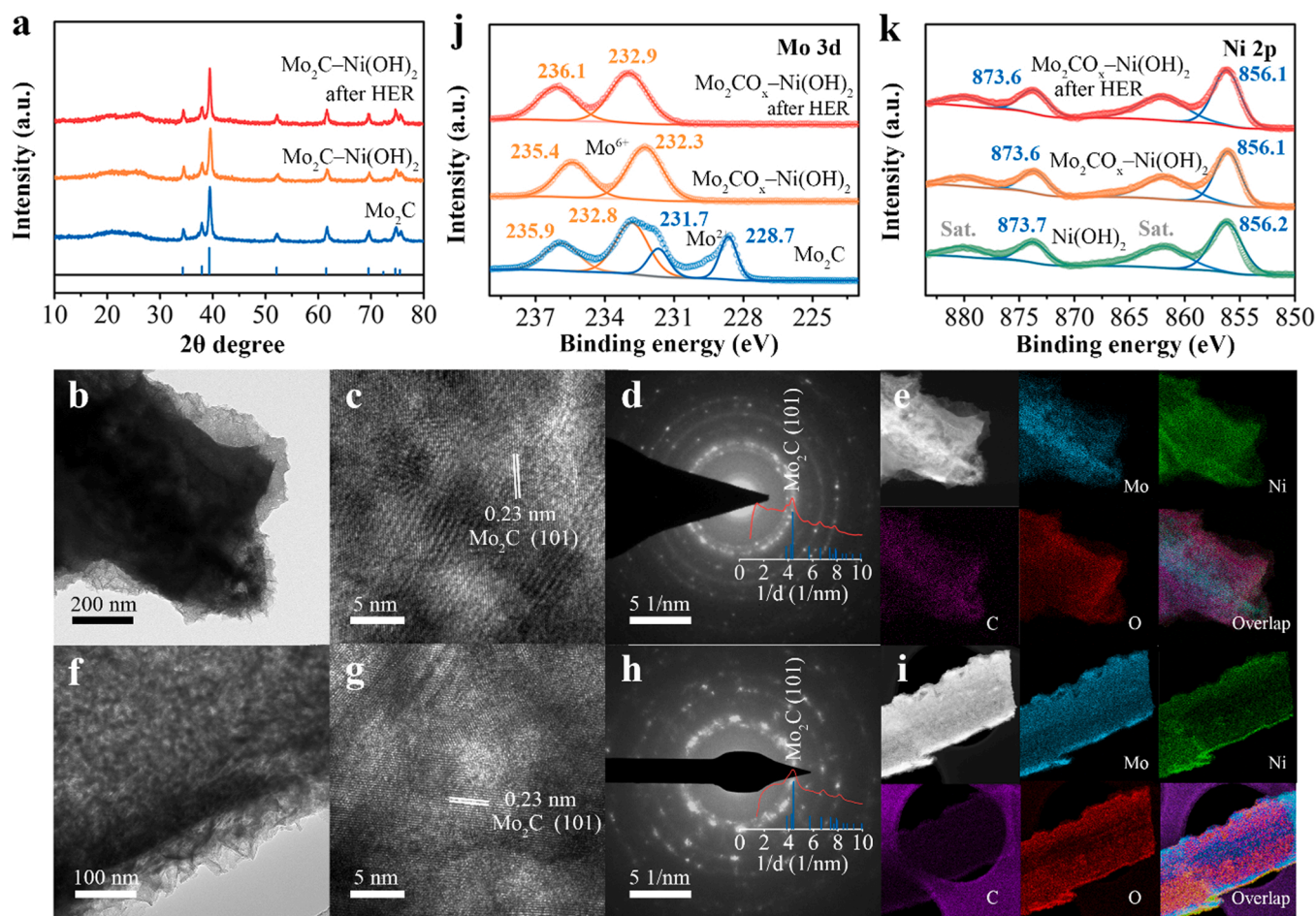
Fig. 2. (a) XRD patterns, High resolution (j) Mo 3d and (k) Ni 2p XPS spectra of Mo₂C, Mo₂C−Ni(OH)₂, and Mo₂C−Ni(OH)₂ after HER. (b,f) TEM, (c,g) HRTEM, (d,h) SAED, and (e,i) STEM-EDX images of Mo₂C−Ni(OH)₂ (b–e) before and (f–i) after HER.

Notably, broad stripes (0.66 nm) in Fig. 2c can be assigned to the (003) plane of Ni(OH)₂•2 H₂O (PDF No. 73-2408), and amorphous domains can also be assigned to amorphous Ni(OH)₂, due to the high crystallinity of Mo₂C after high-temperature treatment. The extracted intensity profile [33] based on the selected area electron diffraction (SAED) pattern (Fig. 2d) matches well with the hexagonal Mo₂C without any signal of Ni(OH)₂, which also reveals its amorphous or low-crystallinity structure. And the energy-dispersive X-ray (EDX) mapping images indicate the uniform distribution of Ni(OH)₂ domains (Fig. 2e). Notably, after HER activation, the corresponding TEM (Fig. 2f), HRTEM (Fig. 2g), SAED (Fig. 2h), and mapping (Fig. 2i) analyses of Mo₂C−Ni(OH)₂ indicate that the phase composition remains almost unchanged. Then we characterized the surface components of the resultant catalysts via X-ray photoelectron (XPS). Note that all samples undergoing the electrodepositions and HER tests were directly transferred to N₂-protected atmosphere for drying to avoid much O₂-induced contamination in the ambient environment. In the fitted Mo 3d (Fig. 2j), the pair peaks at 232.8 and 235.9 eV (Mo $^{6+}$) are assigned to Mo−O signals, and the pair peaks at 228.7 and 231.7 eV (Mo^{2+}) are assigned to Mo−C signals. Notably, the Mo−C signals of Mo₂C after Ni(OH)₂ deposition can be barely observed, which indicates that the electrodeposition process of Ni (OH)₂ triggers the surface oxidation of Mo₂C to Mo₂CO$_x$. Thus, Mo₂C after the electrodeposition process is abbreviated as Mo₂CO$_x$−Ni(OH)₂. In contrast, Mo−S signals of MoS₂ stay nearly unchanged after the electrodeposition, indicating that the surface of MoS₂, unlike the metastable surface of Mo₂C, is quite stable during the electrodeposition process (Fig. S12). Empirically, MoO$_x$ species can be dissolved in the form of MoO₄²⁻ in 1.0 M KOH, and it makes sense that Mo−O signals of

MoS₂−Ni(OH)₂ are obviously reduced after HER (Fig. S12b). However, Mo₂CO$_x$−Ni(OH)₂ after activation performs similar oxidation peaks to Mo₂CO$_x$−Ni(OH)₂, which shows that the surface molybdenum oxides can be well maintained despite that the reaction proceeds in such strong alkaline media. Considering that the reaction proceeds mainly on the surface of the catalysts, it can be inferred that the activation process of Mo₂CO$_x$−Ni(OH)₂ correlates heavily with the surface molybdenum oxides. In the Ni 2p window (Fig. 2k), the fitted pair peaks observed at 856.2 and 873.7 eV are assigned to Ni^{2+}, typical to Ni(OH)₂ in general [10].

Before further speculations, the roles of the surface molybdenum oxides and Ni(OH)₂ for the promoted HER performance should be systematically discussed. Then, we first tested the p-t curve of the Mo₂C for comparison. As shown in Fig. 3a, the pure Mo₂C catalyst shows a deactivation process during HER, which indicates that pure Mo₂C cannot undergo the activation process without the combination of Ni (OH)₂. Note that previous reports have suggested that Mo₂C has a strong affinity with oxygen groups during HER, which is highly likely to result in the O-terminated surface because of its metastable structure [30–32]. However, the XPS spectra of Mo₂C after HER show that the Mo–C signals are well maintained (Fig. 3b). More clearly, Mo₂CO$_x$ was successfully constructed in the same electrochemical process except that 0.2 M KNO₃ instead of 0.1 M Ni(NO₃)₂ was used as the electrolyte. As shown in Fig. S13, the Mo−C signals of Mo₂CO$_x$ after HER are observable, which suggests that it is unlikely that the O-terminated surface with significant O concentrations forms on the pure Mo₂C in such a strong alkaline media. Therefore, molybdenum oxides in Mo₂CO$_x$−Ni(OH)₂ may be peeled off and dissolved into MoO₄²⁻ during the alkaline HER. If so, is
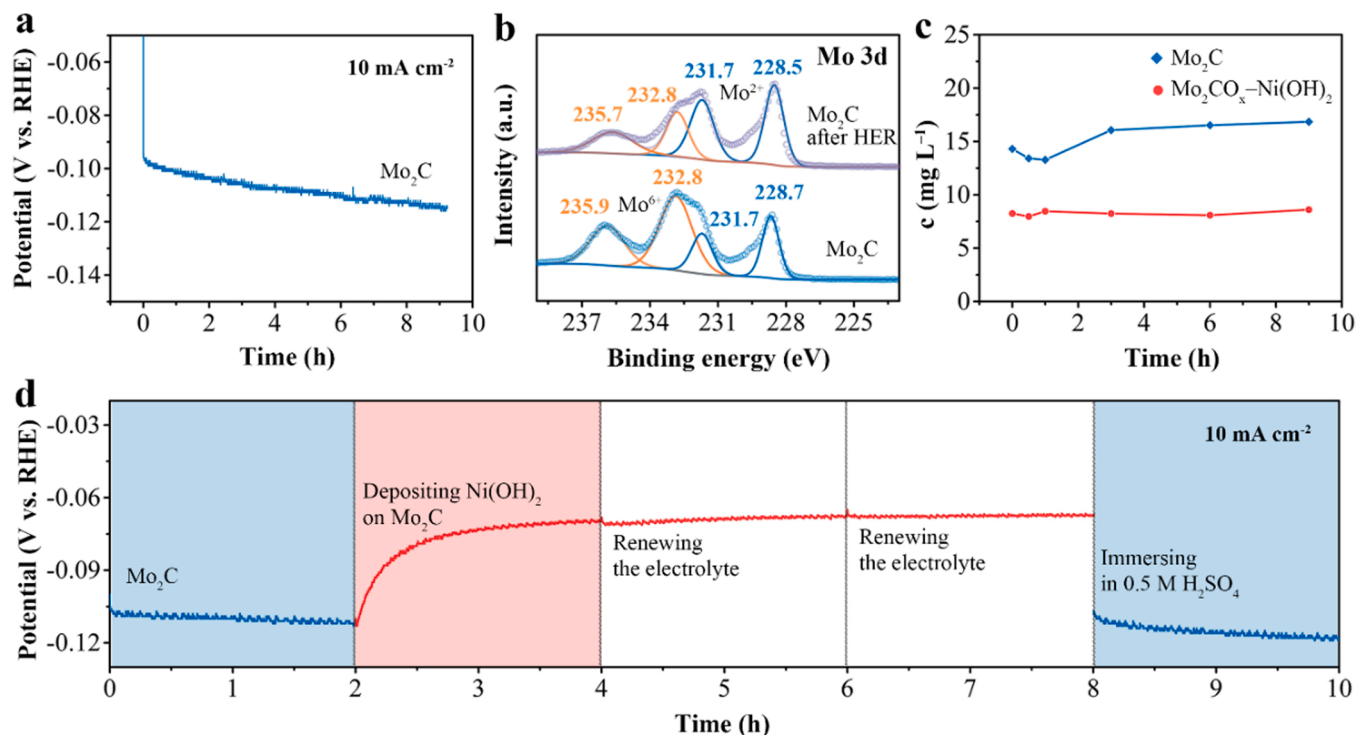
Fig. 3. (a) P–t curve of Mo_2C at 10 mA cm^{-2} for 9 h. (b) High resolution Mo 3d XPS spectra of Mo_2C before and after HER. (c) Time-dependent concentration of dissolved Mo in the electrolyte of Mo_2C and $Mo_2CO_x–Ni(OH)_2$. (d) P–t curves of Mo_2C collected after several operations. 2–4 h: after depositing $Ni(OH)_2$; 4–6 h: renewing the electrolyte; 6–8 h: renewing the electrolyte again; 8–10 h: immersing in 0.5 H_2SO_4 to remove the surface $Ni(OH)_2$.

that possible that the activation process is just simply ascribed to the synergistic effect between $Ni(OH)_2$ and Mo_2C, typical to the classic "dual-site" catalysts? In this regard, we next tested the performance of $Mo_2CO_x–Ni(OH)_2$ just immersed in the electrolyte. As shown in Fig. S14, $Mo_2CO_x–Ni(OH)_2$ after immersion in 1.0 M KOH for 9 h shows no obvious change, indicating that the dissolution of MoO_x species during HER should not be the main reason for the promoted performance. Moreover, the reaction activity of the catalysts may correlate with some ions [34–37], e.g., NO_3^- on the nitrogen reduction [35], Fe^{3+} on oxygen evolution [36], and $Mo_2O_7^{2-}$ on HER [37]. Therefore, we also discussed the relationship between the dissolved MoO_4^{2-} and the promoted performance. As shown in Fig. 3c, the inductively coupled plasma-mass spectrometry (ICP-MS) results indicate that the dissolved Mo in the electrolyte reaches a high content of 14.3 mg L^{-1} when Mo_2C was just immersed in the electrolyte, and increases slowly with time throughout the process. Similarly, the dissolved Mo of $Mo_2CO_x–Ni(OH)_2$ reaches a high content of 8.2 mg L^{-1} when $Mo_2CO_x–Ni(OH)_2$ was just immersed in the electrolyte, and keeps steady as HER proceeds. Indeed, the activated HER performance is not in accordance with the dissolved Mo as HER proceeds. Note that the dissolved Mo content of $Mo_2CO_x–Ni(OH)_2$ is much slower than that of Mo_2C. It can be inferred that the surface MoO_x species are unstable in pure Mo_2C sample, which is likely to lead to the easy dissolution of MoO_x, while the incorporation of $Ni(OH)_2$ can stabilize the surface MoO_x species on Mo_2C in $Mo_2CO_x–Ni(OH)_2$. To further eliminate the effect of MoO_4^{2-} in the electrolyte, the electrolyte of $Mo_2CO_x–Ni(OH)_2$ is renewed twice in the following 4 h after the activation becoming inconspicuous (Fig. 3d), and the well maintained performance indicates that the dissolved Mo is irrelevant to the activation process. When immersing the activated $Mo_2CO_x–Ni(OH)_2$ in 0.5 M H_2SO_4 for 30 min to remove $Ni(OH)_2$, the performance goes worse again. As for the possible transformation of $Ni(OH)_2$, we also tested the p-t curve of $Ni(OH)_2$ for comparison (Fig. S15). Obviously, no activation of $Ni(OH)_2$ indicates that it is not possible that $Ni(OH)_2$ transforms to Ni during HER, since the cooperation of Ni and $Ni(OH)_2$ can lead to an enhanced HER performance. Notably, $Ni(OH)_2$ can

promote the surface wettability of the hybrids (Fig. S16). Correlating the results above, we can infer that the roles of $Ni(OH)_2$ and HER activation are both indispensable, and the dissolved Mo species cannot account for the promoted performance.

Considering that the electrochemical techniques are more sensitive toward the structural alteration, the electrochemical behavior of catalysts are monitored by cyclic voltammetry (CV) test. As shown in Fig. 4a, $Mo_2CO_x–Ni(OH)_2$ after HER shows a reduction peak of about 0.02 V and an oxidation peak of about 0.22 V, and such redox peaks can be ascribed to hydrogen de/intercalation in metal oxides according to previous works [38–40]. Note that the premodified substoichiometric (oxygen vacancies) MoO_x (WO_x) catalysts also show much better HER activities than stoichiometric MoO_3 (WO_3) [41–43], and the formation of vacancies can be understood to result in modified electronic structures, leading to altered HER activities [44,45]. However, it is quite difficult to produce O vacancies with high concentrations at potentials relevant to HER [46]. Rather, metal oxides, in a cathodic electrochemical condition, tend to undergo bulk hydrogen intercalation [38–40,46]. Thus, the in-situ hydrogen intercalation can account for the promoted HER performance, and then $Mo_2CO_x–Ni(OH)_2$ after activation is abbreviated as $H_xMo_2CO_x–Ni(OH)_2$. In comparison, there is no hydrogen adsorption current in the CV curves of Mo_2C and $Mo_2CO_x–Ni(OH)_2$, which further indicates that the hybrid structure and the activation process are both indispensable. And the weak signals in $MoS_2–Ni(OH)_2$ after HER is in accordance with the electrochemical behavior during HER (Fig. S17). Notably, in the previous cases of hydrogen intercalation, the HER tests were performed in the acidic electrolyte, and the hydrogen is derived from the reduction of H^+ and can be inserted into metal oxides [39,40]. If so, in the case of alkaline HER, the low concentration of H^+ suggests that $Ni(OH)_2$ still works in the traditional bifunctional mechanism for providing a local acid-like environment in our work. Additionally, electrochemical double-layer capacitances (C_{dl}) were calculated from the plot of capacitive current against the scan rate to evaluate the active surface area (Fig. 4b, S18, and S19). As shown in Fig. 4b, the C_{dl} values for Mo_2C, $Mo_2CO_x–Ni(OH)_2$, and $H_xMo_2CO_x–Ni(OH)_2$ are 171.0, 137.0,
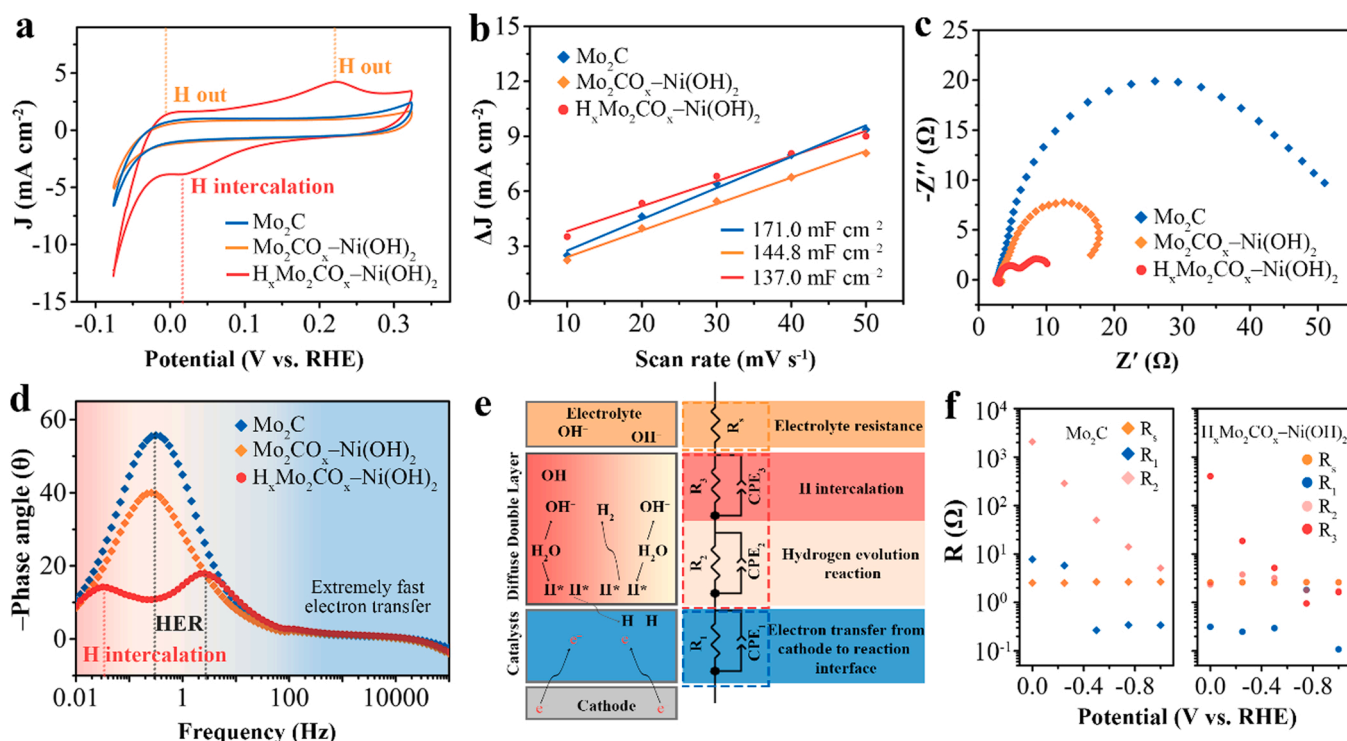
Fig. 4. (a) CV curves, (b) C_{dl} values (c) Nyquist plots, and (d) corresponding Bode plots of Mo_2C, $Mo_2CO_x-Ni(OH)_2$, and $H_xMo_2CO_x-Ni(OH)_2$. (e) The equivalent circuit for $H_xMo_2CO_x-Ni(OH)_2$. (f) Correlation of equivalent resistances (R_s, R_1, R_2, and R_3) and potentials of Mo_2C and $H_xMo_2CO_x-Ni(OH)_2$.

and 144.8 mF cm^{-2}, respectively. Hereinto, Mo_2C exhibits the largest C_{dl} value because of its high active sites, while both $Mo_2CO_x-Ni(OH)_2$ and $H_xMo_2CO_x-Ni(OH)_2$ exhibit quite low C_{dl} values because the inert Ni $(OH)_2$ and molybdenum oxides hinder the exposure of Mo_2C. Notably, the smaller C_{dl} value of $H_xMo_2CO_x-Ni(OH)_2$ than that of Mo_2C indicates that the remarkable activity should not be simply ascribed to the high surface areas.

Note that both hydrogen evolution and hydrogen intercalation correlate with applied potentials, then the electrochemical impedance spectroscopy (EIS) at different applied electrochemical potentials were performed to identify the electrochemical reaction types of $H_xMo_2CO_x-Ni(OH)_2$ and reference electrodes (Figs. S20–S22). Typically, Nyquist plots recorded at the overpotential of 50 mV are shown in Fig. 4c. Hereinto, $H_xMo_2CO_x-Ni(OH)_2$ shows a much smaller circle arc than Mo_2C and $Mo_2CO_x-Ni(OH)_2$, indicating that the electrode system of $H_xMo_2CO_x-Ni(OH)_2$ features the smallest resistances. Meanwhile, two arc sections can be observed in the Nyquist plot of $H_xMo_2CO_x-Ni(OH)_2$, which suggests that the electrode system of $H_xMo_2CO_x-Ni(OH)_2$ features two kinds of electrochemical reaction types. More clearly, these two charge transfer types are identified by the variation of the phase angle in the corresponding Bode plots (Fig. 4d). According to previous works, the signals of the charge transfer with different characteristic frequencies in Bode plots are divided into two regions. In general, the electron transfer on catalyst inner-layer responds in the high frequency area (between 10^2 and 10^6 Hz), while the charge transfer on the catalyst-electrolyte interface responds in low-frequency area (between 10^{-2} and 10^2 Hz) [47–49]. As shown in the high-frequency area, there is no obvious response in all samples with the alteration of frequency, indicating that the catalyst inner-layer electron transfer is extremely fast and the electrolyte-catalyst interface charge transfer governs the electron transfer resistance of HER. The two phase-angle peaks for $H_xMo_2CO_x-Ni(OH)_2$ are both located in the low-frequency area, which indicates that $H_xMo_2CO_x-Ni(OH)_2$ possesses two types of interface charge transfer. The phase-angle peak at the higher frequency area (between 0.1 and 100 Hz) is ascribed to the reaction of the intermediates accumulation

process, which involves HER including the Volmer and Heyrovsky steps [50]. And the new phase-angle peak at a lower frequency area (between 0.01 and 0.1 Hz) can be ascribed to hydrogen intercalation since similar peaks can also be observed in $MoO_x-Ni(OH)_2$ system (Fig. S22). As the H adsorption on Pt can be easily detected, the CV and EIS results of Pt/C can serve as auxiliary supports of H intercalation (Fig. S23). Hereafter, the EIS data were simulated by the equivalent circuit model (Fig. 4e). Generally, the equivalent circuit model consists of three parts: (1) The first parallel circuit involves the constant phase element (CPE$_1$) and the resistance (R$_1$), which is associated with the electron transfer from the cathode (catalyst inner-layer) to the reaction interface; (2) The second parallel circuit involves the constant phase element (CPE$_2$) and the resistance (R$_2$), which responds to interface reaction charge transfer; (3) R$_s$ is interpreted as electrolyte resistance. Particularly for $H_xMo_2CO_x-Ni(OH)_2$, an additional parallel circuit involving the constant phase element (CPE$_3$) and the resistance (R$_3$) is associated with the hydrogen intercalation process. From the data (Fig. 4f and Table S1), the small R$_1$ shows the extremely fast electron transfer ability of Mo_2C, $Mo_2CO_x-Ni(OH)_2$, and $H_xMo_2CO_x-Ni(OH)_2$, which indicates that the deposition of $Ni(OH)_2$ does not impede the fast electron transfer ability of Mo_2C. Notably, $H_xMo_2CO_x-Ni(OH)_2$ shows much smaller R$_2$ of 3.21 Ω than Mo_2C (50.11 Ω) and $Mo_2CO_x-Ni(OH)_2$ (23.96 Ω), revealing the faster HER kinetics of $H_xMo_2CO_x-Ni(OH)_2$. Therefore, the significant role of hydrogen intercalation in accelerating HER kinetics and promoting charge transfer during HER has been revealed. The polarization curves with the ohmic drop are shown in Fig. S24, and the comparison of HER activities of $H_xMo_2CO_x-Ni(OH)_2$ with other representative catalysts is summarized in Table S2. Impressively, the $H_xMo_2CO_x-Ni(OH)_2$ shows remarkable HER performance with the η_{10} of 52 mV and Tafel slope of 55.0 mV dec^{-1}. Moreover, Mo_2C with different morphology was prepared (Figs. S25 and S26), and the related electrochemical behaviors were tested (Fig. S27), which verifies the universality of structural transformations of Mo_2C.

Correlated with the experimental results above, the involved two main steps of surface reconstruction are depicted in Fig. 5a. Firstly, the
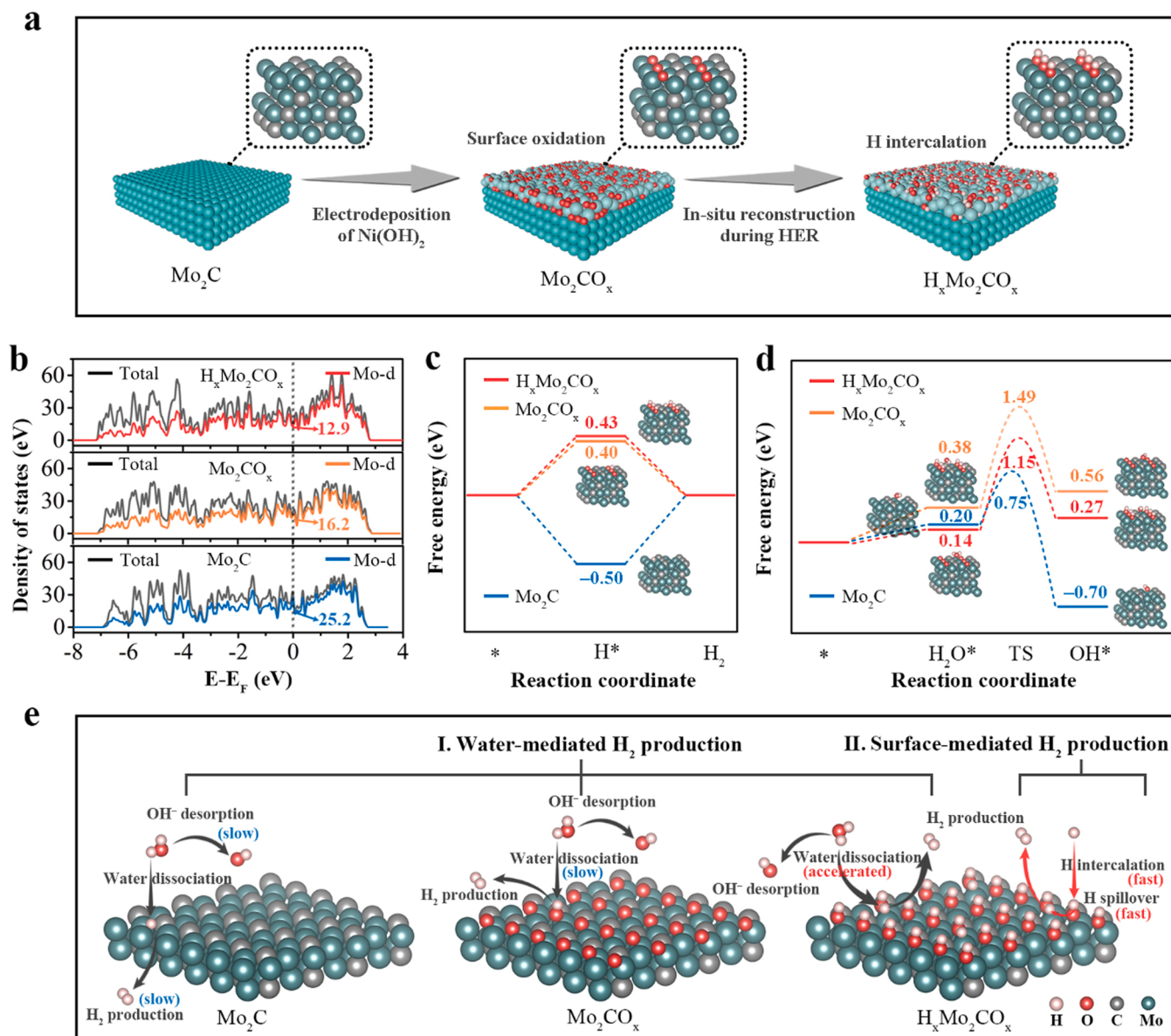
Fig. 5. (a) Illustration for the in situ reconfiguration of $H_xMo_2CO_x$–$Ni(OH)_2$; (b) Calculated density of states (DOSs) for Mo_2C, Mo_2CO_x, and $H_xMo_2CO_x$. (c) Calculated free energies of hydrogen. (d) Calculated free energies of water and hydroxyl species. (e) Simplified proposed reaction pathways for H_2 formation on Mo_2C, Mo_2CO_x, and $H_xMo_2CO_x$.

electrodeposition process of $Ni(OH)_2$ triggers the surface oxidation of Mo_2C to form Mo_2CO_x–$Ni(OH)_2$, and the newly formed $Ni(OH)_2$ works in the traditional bifunctional mechanism, thus providing a local acid-like environment for Mo_2CO_x in the alkaline medium. Subsequently, the HER induced in situ hydrogen intercalation leads to the formation of $H_xMo_2CO_x$–$Ni(OH)_2$, which shows the promoted HER performance. To gain further interpretation for the promoted performance, the in situ hydrogen intercalated Mo_2CO_x is simulated by the commonly used Mo_2C (101) facet as the basic model for DFT calculations. For the simplified oxidation state, Mo_2CO_x is represented by the four-layer 3×4 surface slab of Mo_2C with six oxygen atoms introduced. Note that the interaction between hydrogen and oxygen in metal oxides has been confirmed in previously reported hydrogen intercalation samples [40,46], then we constructed $H_xMo_2CO_x$ with hydrogen atoms introduced at the surface oxygen sites. The optimized structures for Mo_2C, Mo_2CO_x, and H_xMo_2-CO_x are displayed in Fig. S28. We next examined the physical changes of Mo_2C after surface oxidation and hydrogen intercalation. As depicted in Fig. 5b, the density of states (DOS) around the Fermi level show

down-shift from 25.2 to 16.2 and 12.9 after the surface of Mo_2C (101) is terminated by the O atom and the OH group, which indicates the decrease of the electronic activity of the critical Mo atom. For the alkaline HER, the reaction intermediates (H*, H_2O*, and OH* species) play important roles in hydrogen production, water dissociation, and hydroxyl desorption. Herein, the adsorption energies of H*, H_2O*, and OH* are employed as the descriptors for HER activities of the catalysts (Fig. 5c,d and S29−S31). As an initial descriptor, hydrogen binding energies (ΔG_{H*}) for Mo_2C, Mo_2CO_x, and $H_xMo_2CO_x$ are − 0.50, 0.40, and 0.43 eV respectively, indicating that pure Mo_2C surface binds relatively strongly with hydrogen while Mo_2CO_x and $H_xMo_2CO_x$ show quite weak adsorption abilities. And the similar ΔG_{H*} of Mo_2CO_x and $H_xMo_2CO_x$ suggests that hydrogen binding energy is not the key factor for the much better HER activity of $H_xMo_2CO_x$. Therefore, the adsorption energy of H_2O (ΔG_{H2O*}) was next examined. Compared with Mo_2C (0.20 eV) and Mo_2CO_x (0.38 eV), $H_xMo_2CO_x$ shows much favorable adsorption energy of 0.14 eV, which reveals that the water reactant is much energetically favorable for adsorption on $H_xMo_2CO_x$.

Furthermore, the water dissociation and hydroxyl desorption abilities of the catalysts were evaluated by hydroxyl adsorption energy (ΔG_{OH*}) [51,52]. On the weak OH* binding side, water dissociation dominates the kinetics of the Volmer step. Instead, OH* desorption becomes critical. In this regard, similar to ΔG_{H*}, the optimal hydroxyl adsorption free energy (ΔG_{OH*}) is assumed to be about thermoneutral 0 eV. As shown in Fig. 5d, the ΔG_{OH*} for Mo$_2$C is $-$ 0.70 eV, indicating that OH* desorption on the surface of Mo$_2$C during the Volmer step is quite sluggish. However, the positive ΔG_{OH*} value for Mo$_2$CO$_x$ and H$_x$Mo$_2$CO$_x$ suggests that the rate-determining step (RDS) is water dissociation. Notably, the lower energy barrier for water dissociation of H$_x$Mo$_2$CO$_x$ (1.15 eV) than that of Mo$_2$CO$_x$ (1.49 eV) reveals that the H intercalation endows H$_x$Mo$_2$CO$_x$ with much favorable water dissociation kinetics. More clearly, the simplified proposed reaction pathways for H$_2$ formation on Mo$_2$C, Mo$_2$CO$_x$, and H$_x$Mo$_2$CO$_x$ are displayed in Fig. 5e. For pure Mo$_2$C, both hydroxyl desorption during the Volmer step and hydrogen desorption during the Tafel or Heyrovsky step are hindered due to the strong affinities of Mo$_2$C with OH* and H* species. Note, however, that the suggested rate-determining steps have been altered to water dissociation and hydrogen adsorption steps after the surface oxidation, since the terminal O atoms decrease the electronic activity of the critical Mo atoms. For the intercalated Mo$_2$CO$_x$, H intercalation endows H$_x$Mo$_2$CO$_x$ with a favorable water dissociation ability, which accounts for the promoted activity of H$_x$Mo$_2$CO$_x$ regarding the water-mediated H$_2$ production pathway. Meanwhile, H intercalation enables H spillover during H recombination, which provides a fast surface-mediated H$_2$ production pathway.

3. Discussion

In summary, we reveal that Mo$_2$C undergoes two consecutive phase transformations, including the surface oxidation and the hydrogen interaction because of its metastable structure, and demonstrate that the hydrogen intercalated Mo$_2$CO$_x$−Ni(OH)$_2$ hybrid that shows excellent activity for catalyzing alkaline HER. XPS results indicate that the electrodeposition of Ni(OH)$_2$ triggers the surface oxidation of Mo$_2$C, which endows further hydrogen intercalation of Mo$_2$CO$_x$−Ni(OH)$_2$ in the following HER. In-situ cyclic voltammetry and multiple characterizations reveal the electrochemically driven in-situ hydrogen intercalation from Mo$_2$CO$_x$–Ni(OH)$_2$ to H$_x$Mo$_2$CO$_x$–Ni(OH)$_2$, which accounts for the promoted performance as HER proceeds. DFT calculations indicate that the surface oxidation changes rate-determining steps of Mo$_2$CO$_x$ from OH* and H* desorption to water dissociation and H* adsorption by altering H* and OH* adsorption behavior, and the hydrogen intercalation accelerates water dissociation kinetics of H$_x$Mo$_2$CO$_x$ by reducing H$_2$O* and OH* adsorption free energies. Our work unveils the hydrogen intercalation in neglected surface oxides during alkaline HER, and thus provides a deep insight into the performance-enhanced origin under reaction conditions.

CRediT authorship contribution statement

Hong Chuan Fu: Conceptualization, Investigation, Writing – original draft. **Xiao Hui Chen:** Data curation**,** Software. **Bo Yang:** Investigation. **Yuan Hao Luo:** Investigation. **Ting Li:** Visualization, Resources. **Xiao Hu Wang:** Visualization, Resources. **Qing Zhang:** Validation, Software. **Xiao Lin Li:** Validation, Software. **Nian Bing Li:** Supervision, Conceptualization, Funding acquisition, Writing – review & editing. **Hong Qun Luo:** Supervision, Conceptualization, Funding acquisition, Writing – review & editing.

Declaration of Competing Interest

The authors declare that they have no known competing financial interests or personal relationships that could have appeared to influence the work reported in this paper.

Data Availability

Data will be made available on request.

Appendix A. Supporting information

References

[1] L. Wang, C. Lin, D. Huang, J. Chen, L. Jiang, M. Wang, L. Chi, L. Shi, J. Jin, Optimizing the Volmer step by single-layer nickel hydroxide nanosheets in hydrogen evolution reaction of platinum, ACS Catal. 5 (2015) 3801–3806.

[2] Y. Zheng, Y. Jiao, Y. Zhu, L.H. Li, Y. Han, Y. Chen, M. Jaroniec, S.-Z. Qiao, High electrocatalytic hydrogen evolution activity of an anomalous ruthenium catalyst, J. Am. Chem. Soc. 138 (2016) 16174–16181.

[3] J. Wang, F. Xu, H. Jin, Y. Chen, Y. Wang, Non-noble metal-based carbon composites in hydrogen evolution reaction: Fundamentals to applications, Adv. Mater. 29 (2017), 1605838.

[4] Y. Xu, R. Wang, J. Wang, Y. Zhang, T. Jiao, Encapsulation of Fe-CoP with P, N-co-doped porous carbon matrix as a multifunctional catalyst for wide electrochemical applications, J. Energy Chem. 71 (2022) 36–44.

[5] Y. Xu, R. Wang, Z. Liu, L. Gao, T. Jiao, Z. Liu, Ni2P/MoS2 interfacial structures loading on N-doped carbon matrix for highly efficient hydrogen evolution, Green. Energy Environ. 7 (2022) 829–839.

[6] X. Wang, Y. Zheng, W. Sheng, Z.J. Xu, M. Jaroniec, S.-Z. Qiao, Strategies for design of electrocatalysts for hydrogen evolution under alkaline conditions, Mater. Today 36 (2020) 125–138.

[7] Y. Jiang, P. Sun, L. Sharma, B. Mao, R. Kakkar, T. Meng, L. Zheng, M. Cao, Further insights into bifunctional mechanism in alkaline hydrogen evolution for hybridized nanocatalysts and general route toward mechanism-oriented synthesis, Nano Energy 81 (2021), 105645.

[8] R. Subbaraman, D. Tripkovic, D. Strmcnik, K.-C. Chang, M. Uchimura, A. P. Paulikas, V. Stamenkovic, N.M. Markovic, Enhancing hydrogen evolution activity in water splitting by tailoring Li$^+$-Ni(OH)$_2$-Pt interfaces, Science 334 (2011) 1256–1260.

[9] R. Subbaraman, D. Tripkovic, K.-C. Chang, D. Strmcnik, A.P. Paulikas, P. Hirunsit, M. Chan, J. Greeley, V. Stamenkovic, N.M. Markovic, Trends in activity for the water electrolyser reactions on 3d M (Ni, Co, Fe, Mn) hydr (oxy) oxide catalysts, Nat. Mater. 11 (2012) 550–557.

[10] B. Zhang, J. Liu, J. Wang, Y. Ruan, X. Ji, K. Xu, C. Chen, H. Wan, L. Miao, J. Jiang, Interface engineering: the Ni(OH)$_2$/MoS$_2$ heterostructure for highly efficient alkaline hydrogen evolution, Nano Energy 37 (2017) 74–80.

[11] Q. Zhang, W. Xiao, W.H. Guo, Y.X. Yang, J.L. Lei, H.Q. Luo, N.B. Li, Macroporous array induced multiscale modulation at the surface/interface of Co(OH)$_2$/NiMo self-supporting electrode for effective overall water splitting, Adv. Funct. Mater. 31 (2021), 2102117.

[12] H.C. Fu, X.H. Wang, X.H. Chen, Q. Zhang, N.B. Li, H.Q. Luo, Interfacial engineering of Ni(OH)$_2$ on W$_2$C for remarkable alkaline hydrogen production, Appl. Catal. B Environ. 301 (2022), 120818.

[13] M. Miles, M. Thomason, Periodic variations of overvoltages for water electrolysis in acid solutions from cyclic voltammetric studies, J. Electrochem. Soc. 123 (1976) 1459.

[14] J.K. Nørskov, T. Bligaard, A. Logadottir, J. Kitchin, J.G. Chen, S. Pandelov, U. Stimming, Trends in the exchange current for hydrogen evolution, J. Electrochem. Soc. 152 (2005) J23.

[15] W. Sheng, M. Myint, J.G. Chen, Y. Yan, Correlating the hydrogen evolution reaction activity in alkaline electrolytes with the hydrogen binding energy on monometallic surfaces, Energy Environ. Sci. 6 (2013) 1509–1512.

[16] J. Zheng, W. Sheng, Z. Zhuang, B. Xu, Y. Yan, Universal dependence of hydrogen oxidation and evolution reaction activity of platinum-group metals on pH and hydrogen binding energy, Sci. Adv. 2 (2016), e1501602.

[17] I. Ledezma-Yanez, W.D.Z. Wallace, P. Sebastián-Pascual, V. Climent, J.M. Feliu, M. T. Koper, Interfacial water reorganization as a pH-dependent descriptor of the hydrogen evolution rate on platinum electrodes, Nat. Energy 2 (2017) 1–7.

[18] E. Liu, J. Li, L. Jiao, H.T.T. Doan, Z. Liu, Z. Zhao, Y. Huang, K. Abraham, S. Mukerjee, Q. Jia, Unifying the hydrogen evolution and oxidation reactions kinetics in base by identifying the catalytic roles of hydroxyl-water-cation adducts, J. Am. Chem. Soc. 141 (2019) 3232–3239.

[19] B. Mao, P. Sun, Y. Jiang, T. Meng, D. Guo, J. Qin, M. Cao, Identifying the adsorbed hydroxyl transfer kinetics as a descriptor of alkaline hydrogen evolution reaction, Angew. Chem. Int. Ed. 59 (2020) 15232–15237.

[20] C. Lv, X. Wang, L. Gao, A. Wang, S. Wang, R. Wang, X. Ning, Y. Li, D. W. Boukhvalov, Z. Huang, Triple functions of Ni(OH)$_2$ on the surface of WN nanowires remarkably promoting electrocatalytic activity in full water splitting, ACS Catal. 10 (2020) 13323–13333.

[21] H. Vrubel, X. Hu, Molybdenum boride and carbide catalyze hydrogen evolution in both acidic and basic solutions, Angew. Chem. Int. Ed. 51 (2012) 12703–12706.

[22] L. Liao, S. Wang, J. Xiao, X. Bian, Y. Zhang, M.D. Scanlon, X. Hu, Y. Tang, B. Liu, H. H. Girault, A nanoporous molybdenum carbide nanowire as an electrocatalyst for hydrogen evolution reaction, Energy Environ. Sci. 7 (2014) 387–392.

[23] F.X. Ma, H.B. Wu, B.Y. Xia, C.Y. Xu, X.W. Lou, Hierarchical β-Mo2C nanotubes organized by ultrathin nanosheets as a highly efficient electrocatalyst for hydrogen production, Angew. Chem. Int. Ed. 54 (2015) 15395–15399.

[24] H.B. Wu, B.Y. Xia, L. Yu, X.-Y. Yu, X.W.D. Lou, Porous molybdenum carbide nano-octahedrons synthesized via confined carburization in metal-organic frameworks for efficient hydrogen production, Nat. Commun. 6 (2015) 1–8.

[25] Y. Xu, R. Wang, J. Wang, J. Li, T. Jiao, Z. Liu, Facile fabrication of molybdenum compounds (Mo2C, MoP and MoS2) nanoclusters supported on N-doped reduced graphene oxide for highly efficient hydrogen evolution reaction over broad pH range, Chem. Eng. J. 417 (2021), 129233.

[26] Y. Liu, G. Yu, G.D. Li, Y. Sun, T. Asefa, W. Chen, X. Zou, Coupling Mo2C with nitrogen-rich nanocarbon leads to efficient hydrogen-evolution electrocatalytic sites, Angew. Chem. Int. Ed. 127 (2015) 10902–10907.

[27] W. Han, L. Chen, B. Ma, J. Wang, W. Song, X. Fan, Y. Li, F. Zhang, W. Peng, Ultra-small Mo2C nanodots encapsulated in nitrogen-doped porous carbon for pH-universal hydrogen evolution: insights into the synergistic enhancement of HER activity by nitrogen doping and structural defects, J. Mater. Chem. A 7 (2019) 4734–4743.

[28] W. Liu, X. Wang, J. Qu, X. Liu, Z. Zhang, Y. Guo, H. Yin, D. Wang, Tuning Ni dopant concentration to enable co-deposited superhydrophilic self-standing Mo2C electrode for high-efficient hydrogen evolution reaction, Appl. Catal. B Environ. 307 (2022), 121201.

[29] S. Yuan, M. Xia, Z. Liu, K. Wang, L. Xiang, G. Huang, J. Zhang, N. Li, Dual synergistic effects between Co and Mo2C in Co/Mo2C heterostructure for electrocatalytic overall water splitting, Chem. Eng. J. 430 (2022), 132697.

[30] Y. Luo, L. Tang, U. Khan, Q. Yu, H.-M. Cheng, X. Zou, B. Liu, Morphology and surface chemistry engineering toward pH-universal catalysts for hydrogen evolution at high current density, Nat. Commun. 10 (2019) 1–9.

[31] X. Huang, J. Wang, H.B. Tao, H. Tian, Z. Zhang, H. Xu, Unraveling the oxide layer on Mo2C as the active center for hydrogen evolution reaction, J. Catal. 389 (2020) 461–467.

[32] C. Griesser, H. Li, E.-M. Wernig, D. Winkler, N. Shakibi Nia, T. Mairegger, T. Götsch, T. Schachinger, A. Steiger-Thirsfeld, S. Penner, True nature of the transition-metal carbide/liquid interface determines its reactivity, ACS Catal. 11 (2021) 4920–4928.

[33] H. Shi, M. Luo, W. Wang, ElectronDiffraction tools, a DigitalMicrograph package for electron diffraction analysis, Comput. Phys. Commun. 243 (2019) 166–173.

[34] Y. Shi, W. Du, W. Zhou, C. Wang, S. Lu, S. Lu, B. Zhang, Unveiling the promotion of surface-adsorbed chalcogenate on the electrocatalytic oxygen evolution reaction, Angew. Chem. Int. Ed. 59 (2020) 22470–22474.

[35] J. Choi, B.H. Suryanto, D. Wang, H.-L. Du, R.Y. Hodgetts, F.M. Ferrero Vallana, D. R. MacFarlane, A.N. Simonov, Identification and elimination of false positives in electrochemical nitrogen reduction studies, Nat. Commun. 11 (2020) 1–10.

[36] L. Trotochaud, S.L. Young, J.K. Ranney, S.W. Boettcher, Nickel–iron oxyhydroxide oxygen-evolution electrocatalysts: the role of intentional and incidental iron incorporation, J. Am. Chem. Soc. 136 (2014) 6744–6753.

[37] W. Du, Y. Shi, W. Zhou, Y. Yu, B. Zhang, Unveiling the in situ dissolution and polymerization of Mo in Ni4Mo alloy for promoting the hydrogen evolution reaction, Angew. Chem. Int. Ed. 60 (2021) 7051–7055.

[38] G. Meng, H. Yao, H. Tian, F. Kong, X. Cui, S. Cao, Y. Chen, Z. Chang, C. Chen, J. Shi, An electrochemically reconstructed WC/WO2–WO3 heterostructure as a highly efficient hydrogen oxidation electrocatalyst, J. Mater. Chem. A 10 (2022) 622–631.

[39] H. Jiang, J.J. Hong, X. Wu, T.W. Surta, Y. Qi, S. Dong, Z. Li, D.P. Leonard, J. J. Holoubek, J.C. Wong, Insights on the proton insertion mechanism in the electrode of hexagonal tungsten oxide hydrate, J. Am. Chem. Soc. 140 (2018) 11556–11559.

[40] E.V. Miu, J.R. McKone, G. Mpourmpakis, The sensitivity of metal oxide electrocatalysis to bulk hydrogen intercalation: hydrogen evolution on tungsten oxide, J. Am. Chem. Soc. 144 (2022) 6420–6433.

[41] Z. Luo, R. Miao, T.D. Huan, I.M. Mosa, A.S. Poyraz, W. Zhong, J.E. Cloud, D.A. Kriz, S. Thanneeru, J. He, Mesoporous MoO3–x material as an efficient electrocatalyst for hydrogen evolution reactions, Adv. Energy Mater. 6 (2016), 1600528.

[42] T. Zheng, W. Sang, Z. He, Q. Wei, B. Chen, H. Li, C. Cao, R. Huang, X. Yan, B. Pan, Conductive tungsten oxide nanosheets for highly efficient hydrogen evolution, Nano Lett. 17 (2017) 7968–7973.

[43] Y.H. Li, P.F. Liu, L.F. Pan, H.F. Wang, Z.Z. Yang, L.R. Zheng, P. Hu, H.J. Zhao, L. Gu, H.G. Yang, Local atomic structure modulations activate metal oxide as electrocatalyst for hydrogen evolution in acidic water, Nat. Commun. 6 (2015) 1–7.

[44] G. Pacchioni, Oxygen vacancy: the invisible agent on oxide surfaces, ChemPhysChem 4 (2003) 1041–1047.

[45] H. Liu, H. Fu, Y. Liu, X. Chen, K. Yu, L. Wang, Synthesis, characterization and utilization of oxygen vacancy contained metal oxide semiconductors for energy and environmental catalysis, Chemosphere 272 (2021), 129534.

[46] J.B. Mitchell, N.R. Geise, A.R. Paterson, N.C. Osti, Y. Sun, S. Fleischmann, R. Zhang, L.A. Madsen, M.F. Toney, D.-e Jiang, Confined interlayer water promotes structural stability for high-rate electrochemical proton intercalation in tungsten oxide hydrates, ACS Energy Lett. 4 (2019) 2805–2812.

[47] R.K. Shervedani, A.R. Madram, Kinetics of hydrogen evolution reaction on nanocrystalline electrodeposited Ni62Fe35C3 cathode in alkaline solution by electrochemical impedance spectroscopy, Electrochim. Acta 53 (2007) 426–433.

[48] R. Doyle, M. Lyons, Kinetics and mechanistic aspects of the oxygen evolution reaction at hydrous iron oxide films in base, J. Electrochem. Soc. 160 (2013) H142.

[49] C. Xie, W. Chen, S. Du, D. Yan, Y. Zhang, J. Chen, B. Liu, S. Wang, In-situ phase transition of WO3 boosting electron and hydrogen transfer for enhancing hydrogen evolution on Pt, Nano Energy 71 (2020), 104653.

[50] W. Chen, B. Wu, Y. Wang, W. Zhou, Y. Li, T. Liu, C. Xie, L. Xu, S. Du, M. Song, Deciphering the alternating synergy between interlayer Pt single-atom and NiFe layered double hydroxide for overall water splitting, Energy Environ. Sci. 14 (2021) 6428–6440.

[51] B. Zhang, J. Wang, J. Liu, L. Zhang, H. Wan, L. Miao, J. Jiang, Dual-descriptor tailoring: the hydroxyl adsorption energy-dependent hydrogen evolution kinetics of high-valance state doped Ni3N in alkaline media, ACS Catal. 9 (2019) 9332–9338.

[52] I.T. McCrum, M. Koper, The role of adsorbed hydroxide in hydrogen evolution reaction kinetics on modified platinum, Nat. Energy 5 (2020) 891–899.